Available online at www.sciencedirect.com
ScienceDirect
C. R. Physique 9 (2008) 184–196
COMPTES RENDUS PHYSIQUE
http://france.elsevier.com/direct/COMREN/

Recent developments in terahertz optoelectronics/Développements récents en optoélectronique térahertz

Metamaterials and infra-red applications

Didier Lippens

Institut d'électronique de microélectronique et de nanotechnologie, Université des sciences et technologies de Lille, UMR CNRS 8520, avenue Poincaré, BP 60069, 59652 Villeneuve d'Ascq cedex, France

Available online 20 February 2008

Abstract

We review the electromagnetic properties of metamaterials aimed at operating at infra-red wavelengths, keeping their potential applications in mind. Split ring resonators and periodically loaded transmission lines are considered with the main emphasis on the guide lines, design rules and characterization techniques. In this context, we address the various routes towards pushing up the operating frequency in the mid- and near- infrared region, with special attention on the breaking of scaling rules and on the technological challenges for metal and full dielectric approaches. ***To cite this article: D. Lippens, C. R. Physique 9 (2008).***

Résumé

Méta-matériaux pour les applications dans l'infrarouge. Nous donnons une revue des propriétés électromagnétiques des méta-matériaux conçus pour fonctionner dans le domaine infrarouge, en tenant compte de leurs applications potentielles. Nous présentons des dispositifs formés de résonateurs à anneaux métalliques fendus et des lignes de transmission à charge périodique, en insistant sur les aspects de guidage des ondes, sur les règles de design des structures et les techniques de caractérisation. Nous expliquons comment atteindre des fréquences de fonctionnement dans le moyen et lointain infrarouge en brisant des règles d'échelle, et en décrivant les challenges technologiques à résoudre, que l'on choisisse des solutions techniques avec des structures métal/diélectrique ou entièrement diélectriques. ***Pour citer cet article : D. Lippens, C. R. Physique 9 (2008).***

Keywords: Negative refractive index materials; Metamaterials; Infra-red; Split ring resonators; Periodically loaded transmission line; Electro-optic sampling; Terahertz technology; Photonic crystals

Mots-clés : Matériaux à indice de réfraction négatif ; Méta-matériaux ; Infrarouge ; Ligne de transmission à charge périodique ; Échantillonnage électro-optique ; Technologie terahertz ; Cristaux photoniques

1. Introduction

Electromagnetic metamaterials are now attracting much interest owing to their unique properties afforded by the achievement of negative values of their permittivity and permeability. An illustration of this novel context is depicted in Fig. 1 which gives the various possibilities resulting from the sign and magnitude of the real part of the effective permittivity (ε_r) and permeability (μ_r) respectively.

When ε_r and μ_r are both positive, extreme values of the relative permittivity and permeability can be achieved via the use of ferroelectrics and ferromagnetics either in thin film or bulk technology. Also, micro- and nano-technologies

E-mail address: Didier.lippens@iemn.univ-lille1.fr.

1631-0705/$ – see front matter
doi:10.1016/j.crhy.2007.07.006

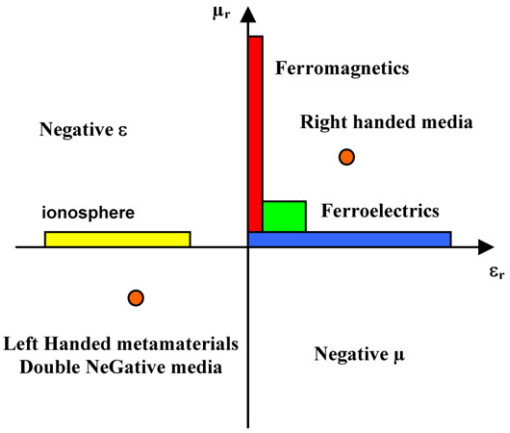

Fig. 1. The openness of effective parameter space.

can now be used to structure artificially matter on a scale much smaller that the wavelength of the interacting electromagnetic wave. It can be shown that such structuring technique impacts considerably the electromagnetic properties of these artificial media. It is now possible to synthesise micro- and nano-structures which exhibit permittivity and permeability values below unity, paving the way for an improved control of electromagnetic waves. In particular, this opens the route for ultra-refraction.

Negative values of ε_r while μ_r remains positive can be obtained with metals, or more generally, with plasma systems. Ionosphere effects are of the most natural examples. In fact, it is well known that the frequency dependence of the permittivity of a metal obeys a Drude dispersion law. The corner frequency between reflectivity and transparency is the so-called plasma frequency which is related to the square root of the electron density in the metal. Therefore, a simple means to decrease the plasma frequency (f_p) is to lower the density of electrons. This can be obtained by using a highly doped bulk semiconductor or a two-dimensional electron gas. Also, it can also be shown that f_p is inversely proportional to the square root of the effective mass of electron. As a consequence, the fabrication of wire arrays will change dramatically the value of the plasma frequency with an increase of the electron effective mass (inductance effect). In conclusion, structuring matter affects the net density of electron via the filling factor of metal wires in a host medium and the effective mass.

The region where μ_r is negative while ε_r is positive allows one to consider electromagnetic media which exhibit an artificial magnetism, via non-metallic microstructures. To this aim, it is imperative to organize matter so that the magnetic response (**B** vector) shows a phase-shift of π with respect to the magnetic field **H**. The most popular route is based on the fabrication of micro-resonators termed Split Ring Resonators (SRRs). Despite the various shapes which can be found in the literature (double rods, edge- or broad-side coupled SRRs, omega or S-type structures, ...) basically the metal inclusion resonates at a characteristic frequency and exhibits a negative value of μ_r above this resonant frequency. Both $\varepsilon_r < 0/\mu_r > 0$ and $\varepsilon_r > 0/\mu_r < 0$ media are termed Single NeGative (SNG) materials. Under these conditions, the electromagnetic waves cannot propagate within the electromagnetic structure because the **k** vector is imaginary. As a consequence, a wave impinging onto such a SNG is reflected. This reflection is soft in the sense that the wave penetrates more or less within the metallic structure. Mathematically, the wave is evanescent close the interface over a distance which depends notably on the angular frequency which defines a forbidden gap. Metallic Photonic Band Gaps (PBGs) belong to this material class. If we fabricate an ultra-thin slab of such a SNG material, a certain transmissivity can be obtained in a manner similar to electron tunnelling through ultra-thin potential barriers in semiconductor heterostructures. In most applications however, these media are used to fabricate electromagnetic mirrors and more importantly to synthesize double negative media.

When the values of ε_r and μ_r are both negative, it can be shown that the real part of the refractive index is negative (negative solution of $n = \pm\sqrt{\varepsilon_r \mu_r}$). This impacts the propagation of waves, which is backward in this case. Physically, this means that the phase fronts propagate in a direction opposite to that of energy flow. Mathematically, this means that the k-vector and S (Poynting) vectors have opposite signs. As a consequence, the trihedron **E** (electric field vector), **H** (magnetic field vector) and **k** (wave-vector) is indirect. This inversion in **k** orientation justifies the

term of Left Handed Materials (LHM). In the following, we will also use the term of Right Handed Materials (RHM) in order to depict the propagation in conventional media.

The purpose of this article is to review the electromagnetic properties of the so-called metamaterials. The prefix meta means beyond. Indeed these materials are artificial ones and structuring them on a scale much smaller than the wavelength yields electromagnetic properties which differ from their constitutive materials. The literature on this subject is now very abundant. In particular, the reader can find a synthesis for microwave metamaterials in [1–21]. In the present work, we will emphasize the challenges for fabricating such Negative Refractive Index Materials (NRIM), a term which is quite general, with special attention to the Infra-Red (IR) spectral region. We will begin from millimeter-waves (around 100 GHz) (defence and space applications) up to the Near-Infra-Red (NIR) region (1.5 μm telecommunication systems). For the latter, it can be shown that the use of a metal structure becomes more and more challenging and as a consequence a full dielectric photonic crystal technology is a good alternative for the observation of negative refraction. In the various frequency bands, millimetre-wave in Section 2, Far-Infra-Red (FIR) in Section 3, Mid-Infra-Red (MIR) in Section 4 and Near-Infra-Red (NIR) in Section 5, we will try to point out the common denominators. The basic concepts, as outlined in the introduction, are applicable over the whole spectrum. However, it will be seen that the magnitude of various effects varies notably with frequency. This is the case for the effect of the so-called intrinsic self-inductance. Also, we will exemplify the technological difficulties notably the fact that structuring matter on a scale much shorter that the wave length is sometimes problematic especially in the NIR. Finally, the difficulties encountered in the characterization of NRIMs will be illustrated. Indeed, most of the expected effects are phase-related so that a vectorial network analysis is often needed.

2. Split ring resonators at millimeter-waves

Fig. 2 gives a picture of the basic cell of a NRIM aimed at operating around 100 GHz. Basically, this is a DNG medium which is fabricated from SRR and wire arrays. We saw in the introduction that a wire array permits one to engineer the value of the plasma frequency via the filling factor of metal wires (here metal strips 'diluted' in a host glass substrate). Artificial magnetism and hence a negative value of μ_r is achieved via the ring-shaped metal inclusion. There are two rings instead of one. Their slits (very narrow in the present case) are opposite. Indeed, it can be shown that a single SRR has a magneto-electric response. This means that both **H** (polarized along z) and **E** (polarized along y) induce some currents in the metal loops. In other words, a single SRR exhibits a bi-anisotropic response. In order to avoid such dual response, the currents induced by the electromotive force resulting from **E** have to cancel. Fig. 3 is an optical view of the prototype fabricated at the University of Bilkent [22].

The requirement that **H** polarization is along z and as a consequence in a direction perpendicular to the substrate is very stringent. This means that the fabrication of such an artificial medium needs to assemble several substrate layers (here 100 substrates). In the microwave spectral region, such an assembling is not a problem. Indeed most of the structure operating for instance in X-band (8–12 GHz) are fabricated by using a Printed Circuit Board (PCB) technology. By increasing the operating frequency, it is imperative to shrink the dimension of basic cells. The fabricated samples are however characterized in free space and the lateral dimensions have to be larger than the beam waist. For instance the diameter of rings is around 200 μm for a side of the 'bulk' sample of the order of 1 cm.

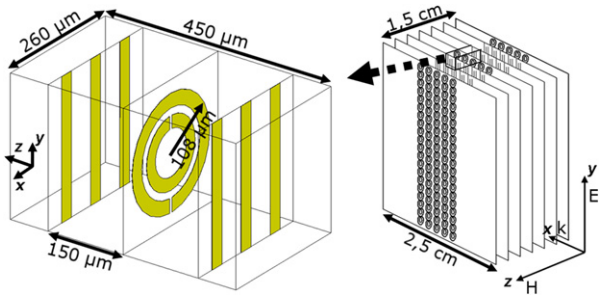

Fig. 2. Basic cell and relevant dimensions.

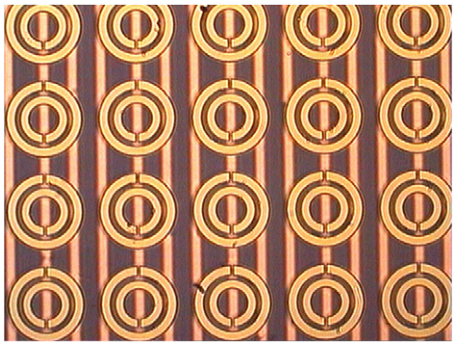

Fig. 3. Optical view of the prototype.

In a first approximation, the dimension of the SRRs can be chosen by describing the micro-resonator by means of their equivalent circuit. Intuitively for a single SRR, one can expect a localization of the electric interaction with the structure in the gap opened between the C-shaped metal patterns. Therefore, the slit (gap) of the ring are equivalent to a lumped capacitance. On the other hand, the round shaped strip is equivalent to an inductance. In conclusion, the resonant response can be described by means of a simple resonant circuit constituted of geometrical inductance and capacitance. This means that the operating frequency can be adjusted by scaling the dimensions of the structure and by keeping in mind that all the relevant dimensions of inclusions have to be much shorter that the wavelength. The wavelength in free space at 100 GHz is 3 mm, the largest dimension (SRR diameter) is around 300 μm. We thus obtain a 10:1 ratio. The same reasoning at 300 THz, 1-μm wavelength corresponding to NIR systems, means that the SRR diameter should be on a submicron scale. We will see that this scaling rule is not correct because other inertia effects described by an intrinsic self inductance have to be introduced. At 100 GHz these effects are negligible, however, and hence an estimate of the resonance frequency, on the basis of the sole geometry of metal inclusion, is correct.

Fig. 4 shows the frequency response of such a structure under free space condition for various numbers of rows along the propagation direction. It can be seen that a single row prototype exhibits an anti-resonance and a resonance peak. The latter is here centred around 107 GHz. By increasing the number of cells to 3 and 5, it can be noted that a pass-band is formed, the rejection is increased but more importantly the insertion losses are dramatically increased in the pass-band. The loss level is plotted in inset as a function of the number of cell. The behaviour is not trivial and depends of the electromagnetic environment of each cell. In any case, it can be noticed that the transmission level is dramatically decreasing and reaches a value around -10 dB for a 4-cell prototype. Therefore one of the first conclusions is the following. NRIM made of SRRs exhibit remarkable effects by tailoring the frequency response. However, due to the resonant nature of inclusions, the loss level is tricky for many applications and a trade-off has to be found between efficiency and losses.

In Fig. 4, the magnitude of the transmission coefficient (S_{21}) has been plotted as a function of frequency. We learnt from this figure that the microstructure exhibits a pass-band around 100 GHz. It remains to demonstrate that this pass-band is left-handed and thus that the artificial structure is a LHM. To show this, one of the most elegant ways is to use the so-called retrieval technique. This means that we extract some frequency variations of ε_r and μ_r from the electromagnetic behaviour. At the moment, there are two techniques in order to perform this extraction. The first one is called Fresnel Inversion (FI) technique [23]. In short, it consists of retrieving the values of ε_r and μ_r which give the frequency dependence of the transmission (S_{21}) and reflection coefficient (S_{11}). The other technique is called Field Summation (FS) technique [24]. It consists to average the field excitation (**H**, **E**) and the field response (**B**, **D**) over some specific surfaces and the volume of the basic cell.

Fig. 5 shows the results of the extraction of the real and imaginary parts of the refractive index, for the 100 GHz prototype described above. With FS technique, the frequency variation follows the dispersion characteristics. The highest negative value is close to -12 vanishing for a frequency around 110 GHz.

A FI technique gives similar results from 107 to 110 GHz. It can be seen however that the real part of the refractive index shows a plateau around -4.5 from 97 to 107 GHz. This plateau reflects the fact that artificial matter is not

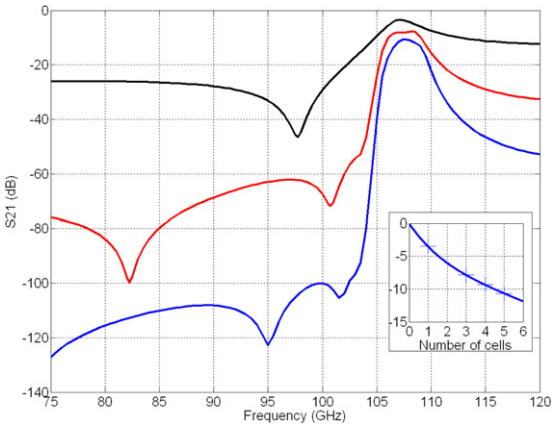

Fig. 4. Transmission characteristics.

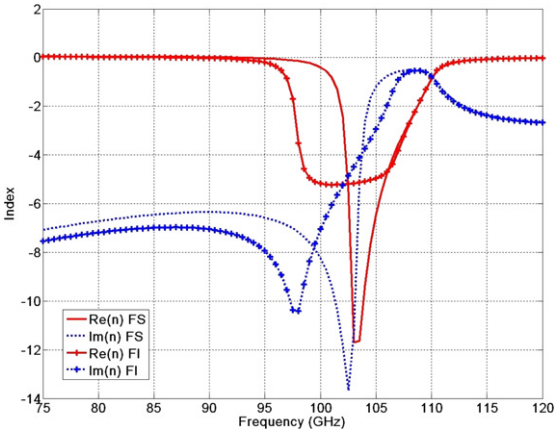

Fig. 5. Dispersion characteristics.

homogeneous. In order words, this means that the electromagnetic wavelength of the wave propagating within the material is no longer large with respect to the relevant dimensions. In conclusion, the electromagnetic wave saw in this frequency range the periodicity of the structure. With respect to the imaginary part, they show peaks for both methods around the resonant frequency which are at the origin of the high level of losses aforementioned. In the next section, we will see how to alleviate the problem of losses using a periodically loaded transmission line approach.

3. Periodically loaded transmission lines at Far-Infra-Red

Fig. 6 shows an optical view of a Transmission Line (TL) loaded periodically by series parallel plate capacitances (the large metallic square shaped plates apparent on the metal strips) and by shunt inductances (the narrow meander shaped wire interconnecting the two strips). The period here is 30 μm for a targeted operating frequency at sub-millimetre wave range (terahertz spectral region). In practice, microelectronics techniques have been used for printing the metal pattern on a thin quartz substrate in order to avoid substrate spurious propagation. The pattern of the self inductance (0.2×0.2 μm^2) cross-section was written by e-beam lithography. The 0.5-μm thick dielectric layer was carried out by plasma enhanced vapour deposition of Si_3N_4 epilayers and the metal layers (strip and pads) were deposited by gold evaporation.

Fig. 7 shows the dispersion diagram which can be calculated by considering a unit-cell and by applying the Bloch Floquet theorem. In short, we calculated the transmission (S_{21}) and reflection characteristic (S_{11}) of a one period cell. The S_{21} and S_{11} scattering parameters are then converted into a chain matrix. Finally, the chain matrix elements are compared to those of a transmission line whose propagation is characterized by a complex propagation constant ($\gamma = \alpha + j\,.\,\beta$). The results for the terahertz prototype outlined above are plotted as a function of frequency versus the phase shift along one unit cell ($k\,.\,a$ where a is the unit cell length). For a real k ($k = \beta$) the dispersion characteristics were plotted for negative value thus for a negative sign of the phase velocity $vp = \omega/k$. Also plotted is the dispersion characteristics which correspond to free space condition namely $\omega = c\,.\,k$ where c is the speed of light. Just to recall that this characteristic defines the so-called light line or light cone. In a superluminal regime, and thus above the light cone, it can be shown that the waves are radiated. This regime corresponds to leaky waves. Below the light cone the wave are guided along the line and it can be shown that the group velocity ($v_g = \partial\omega/\partial k$) is positive. As a consequence the propagation along the line is backward.

Below and above the frequency window for which the propagation media is left-handed and which behaves as a DNG medium, there exist two forbidden bands. They correspond to a SNG situation and the attenuation of the evanescent wave are now depicted by a purely imaginary part of $k = j\alpha$. The attenuation depth depends strongly on the frequency notably around the turning frequencies, 0.15 THz and 0.4 THz respectively.

In order to have direct evidence of the fact that the propagation is backward we will here consider the propagation of a pulse along the line rather than an analysis by means of a network analyzer. With this aim we employed an electro-optic sampling technique in a pump probe scheme. Briefly, this means that we create a short electrical pulse

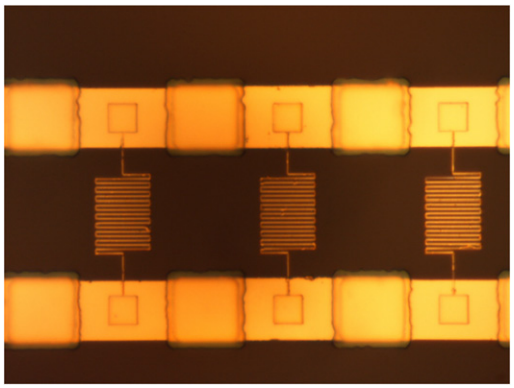

Fig. 6. Optical view of a left-handed transmission line.

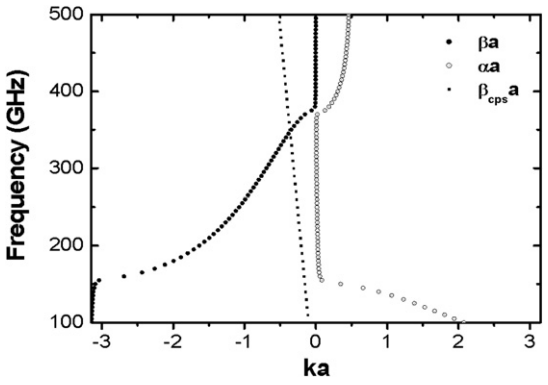

Fig. 7. Dispersion characteristic of the periodically loaded TL. The dispersion branch for negative k is left-handed. Also plotted is the light line. For positive k, the waves are evanescent and characterized by α.

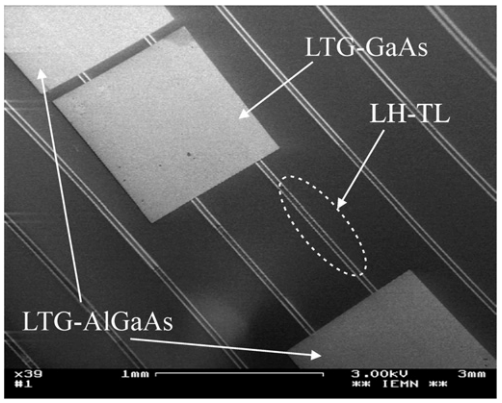

Fig. 8. Scanning Electron Microphotograph (SEM) of a LH transmission line.

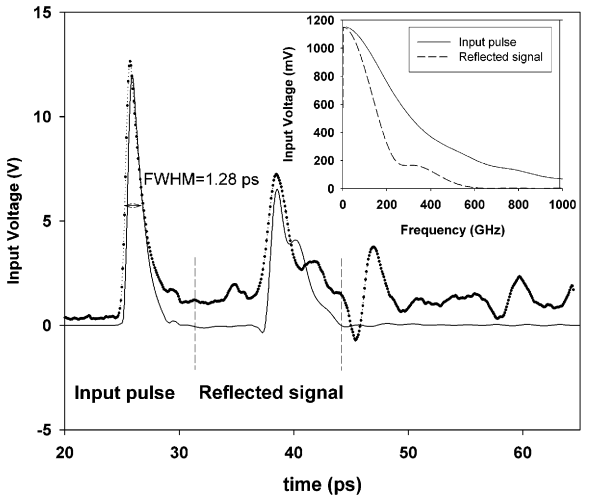

Fig. 9. Time analysis of the reflected waves. Measurements (dotted lines), simulation (solid line).

travelling along the line which is then recorded by keeping the phase information between the pump and the probe sections. The spectral density of the electrical pulse has to be as broad as possible and at least with significant energy in the terahertz Fourier terms. To this goal, we used a femtosecond laser source with a pulse width around 100 fs. This optical pulse illuminated a patch of low temperature grown GaAs semiconductor which is wafer-bonded by Van de Waals force onto the line. A photo of the device is shown in Fig. 8. Also apparent in this figure are two other AlsGaAs patches. They are used for the recording of the reflected and transmitted waves. The detection is made taking benefit of the Franz Keldysh effect in semiconductor. Indeed by using a wider gap semiconductor such as AlGaAs with respect to that of GaAs, carrier absorption can only take place when a high electric field assists the absorption mechanism. As a consequence, by monitoring the absorption process, in practice by a photodiode, the time, when the reflected and transmitted wave reach the patch, can be measured accurately.

Fig. 9 shows the time variation of the pulse recorded experimentally in the input section (on the left-hand side of the previous figure with a GaAs and an AlGaAs patch). We first record a sharp pulse which reflects the pulse launched on the transmission line. Full width at half maximum is around 1 ps. The spectral density is plotted in continuous line in inset. Significant Fourier terms can be found up to 1 THz. In dashed line is plotted the reflected wave coming from the device under test (analysis of the time variation of the reflected signal between 35 and 45 ps). The spectral density is much concentrated below 0.2 THz. This reflection, which is pronounced below 0.2 THz, results from the low frequency forbidden gap. The other features in the time variations at longer time scale are due to spurious reflections at the open ends of the device. These features are also retrieved in the calculated time variations (solid line).

Let us now consider the transmitted wave. The time variations of the signal monitored in the output section on the right hand side of Fig. 8 are displayed in Fig. 10. Instead of a pulse-like waveform the transmitted signal is exhibit an oscillating form with a pseudo period around 3 ps. As expected, the lines behave as a pass-band filter whose spectral density is shown in the insert of Fig. 10. It can be shown that this pass band fits the dispersion characteristic for which the material is left handed. A direct experimental clue of the backward propagation can also brought by comparing the phase shift between two lines. The reader can find further details on this technique in [25].

The first practical application of metamaterial based transmission line is filtering. Indeed, an estimate of losses shows that there are quite reasonable with respect to SRR approaches. For the present device, the loss per cell is around 0.5 dB per cell. Also a significant phase shift can be obtained even with a limited number of cells and more importantly TL's exhibit a phase advance. This opens the way for composite transmission lines as has been successfully demonstrated at microwave wavelengths. The underlying idea is either to combine a LH propagation section, series integrated with a RH propagation medium (conventional transmission line), avoiding by this means the problem of leaky wave above the light cone. Another perhaps more promising solution is to engineer the parameter of the line so that the gap between the LH dispersion branch and the RH dispersion branch vanishes. Under this condition of balanced composite materials, the phase shift can be null at $k = 0$ and $\omega \neq 0$ with a non-vanishing group velocity.

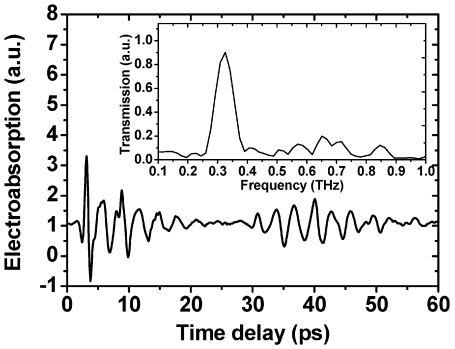

Fig. 10. Time analysis of the transmitted wave.

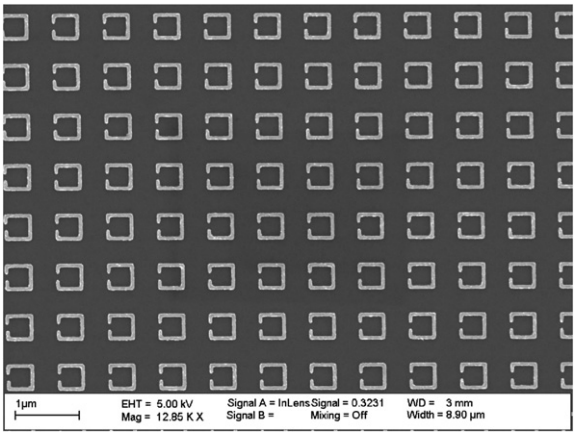

Fig. 11. SEM of a plasmon resonator array.

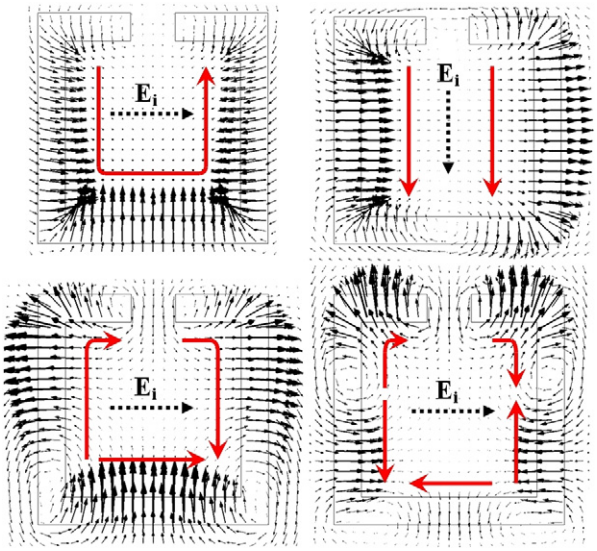

Fig. 12. Illustration of resonance modes.

At last, one can take advantage of the leaky waves above the light cone in order to fabricate a leaky wave antenna whose radiation diagram can be steered over a large scan angle taking benefit of both LH and RH dispersion branches.

4. Plasmon resonator at Mid-Infra-Red

Let us now consider single C-shaped structures aimed at operating at mid infra red shown in Fig. 11.

The scalebar (1 µm) is given on the bottom of the figure. It can be seen that the square-shaped micro-resonator displayed here are fabricated on a submicron scale (400 nm for the side of micro-resonator whereas the width of the slit and metal strip is 80 and 50 nm respectively). For these submicron dimensions, it is imperative to use high resolution lithography technique. In practice the pattern were written by e-beam lithography with a 50 kV accelerating voltage and a 100 nm-thick 950 K PMMA sensible resist. The substrate used for patterning and subsequent gold evaporation is made of a 500 µm-thick Semi Insulating (SI) GaAs which is carefully polished on each side in order to avoid light diffusion. The deposition of a 30 nm-thick gold layer was carried out by evaporation using a conventional lift off technique. We chose a square arrangement for the lattice of the SRR array with a period of 80 nm.

Fig. 12 illustrates the various resonance modes of the micro-resonators as a function of the polarization of the E field. Also plotted is the magnitude of H field (in logarithm scale) which reflects the current modes. The fundamental mode corresponds to the left-hand figure on top. Here, the **E** field is oriented along a split-bearing arm. This allows, by electromotive force, to induce current flows in the current loop illustrated by the arrows shown in this figure. There are no currents induced by the magnetic field **H** because we assume a plane wave impinging onto the SRR

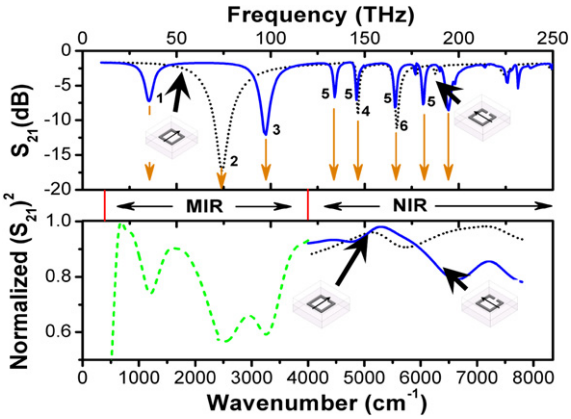

Fig. 13. Comparison between the experimental transmission measured by FTIR and calculated by full wave analysis (upper curve).

array at *normal* incidence. As a consequence, the **H** vector points in a direction parallel to the substrate which holds the single-plane SRR array. The interaction of light with metal inclusions induces plasmon waves at the interfaces between metal and the embedding media. Using this plasmon concept, it can be seen that the ground state corresponds roughly to the matching of the half wavelength to the unfolded length of the micro-resonator. The right hand picture on top corresponds to a second mode when the electric field is rotated by $\pi/2$. In this case, the currents in two adjacent branches are flowing in opposite directions and allow to define two nodes one in the vicinity of the gap and the other in the opposite arm. The two figures at the bottom correspond to the eigen-states of the plasmon resonators characterized by the index # 3 and # 5 respectively in Fig. 13. Identification is based on the same reasoning namely the evidence of 3 and 5 nodes respectively along the electrical path. The **E** polarisation is identical to that of Fig. 1.

In order to characterize experimentally the various resonance modes illustrated by the field mapping reported above, the transmission of a SRR array was measured using a FTIR experiment. A commercial set up allows the use of two kinds of light source which are not linearly polarized. At NIR, however, an external polarization grid is available. The results of this characterization were plotted over the NIR and MIR spectral region in Fig. 13(b). The measurement of the transmissivity is differential. Indeed, we performed the ratio between the transmission spectra without and with the SRR array by means of two different samples. The reference sample is a gold frame which acts as a 5×5 mm^2 diaphragm. By recalling that the basic cell dimensions are 800×800 nm^2 this means that the array has 40 millions of basic cells. From Fig. 13(b) it can be seen that three well-resolved peaks can be identified in the spectral response at MIR at 1200, 2500 and 3300 cm^{-1}.

Surprisingly, the most pronounced peak is not the ground one but the second one. Changing the light source in order to reach the NIR region shows some features in the frequency dependence of the transmission, but with a much weaker contrast along with a broadening. In order to further explain this difference in magnitude and also to see whether the resonant frequency are correctly described by a plasmon resonator model, full wave electromagnetic simulations (High Frequency Structure Simulator by Ansoft) were conducted by introducing the frequency dispersion of the gold layer used for the fabrication of the present prototype. In introduction, we saw that metal layers obey a Drude law with the plasma frequency f_p acting as a turning frequency between reflectivity and transmissivity. For bulk Gold, the plasma frequency is around 2175 THz. However for ultra-thin epilayers (the metal thickness is here of 30 nm) some deviations with respect to this reference value can be expected. Therefore in practice, we took f_p as a parameter modifying by this means the permittivity value and hence the conductivity of metal layer. We also saw that the experiments at MIR were performed without the possibility to linearly polarize the incident light despite the fact that the polarization conditions are crucial as seen on the basis the field mapping. As a consequence, the transmissions as a function of wave number, shown in Fig. 13(a), were calculated separately for the two polarizations of electric field, **E** parallel to the gap bearing arm (solid line) and perpendicular to it (dashed line).

For a fitting value of plasma frequency of 2850 THz, a good agreement was obtained between experimental and calculated extinction peaks at MIR. At NIR, despite the fact that a polarization grid was available experimentally, the features were too weak and broadened to have a meaningful comparison. At this stage, we have to stress that the so-called inertia effects are included in the full wave simulation provided that we introduce the Drude variation

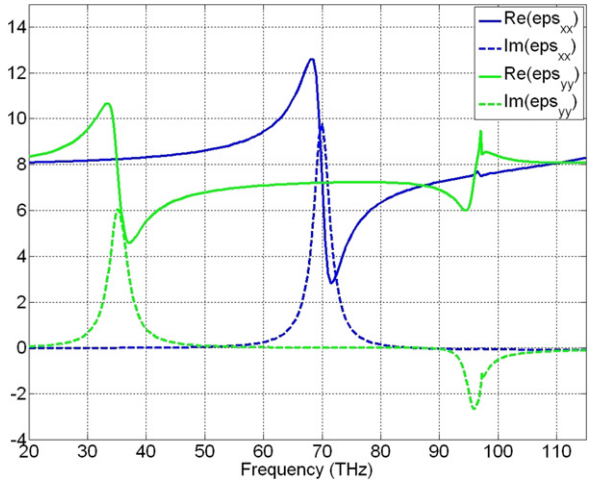

Fig. 14. Field summation technique applied to single SRR.

of the permittivity $\varepsilon_r = 1 - (\omega_p/\omega)^2$ where ω_p is the angular plasma frequency. Indeed, it can be demonstrated that these inertia effects which correspond to the introduction of an intrinsic inductance [26] ($L = L_{\text{eff}}/(\varepsilon_0.w.h.\omega_p^2)$ where L_{eff} is the effective length of micro-resonator, w and h are the width and thickness of the metal strip, the other parameters having their conventional meaning). At the frequency of interest the inertia effects start to decrease the resonant angular frequencies of SRRs ($\omega_r = (C_g(L_g + L_i))^{-1/2}$ where C_g and L_g are the geometrical capacitance and inductance respectively and L_i the intrinsic inductance.

At this stage, it can be seen whether the extraction parameter method outlined in Section 2 notably field summation technique can help us to bring more quantitative information. The results of these calculations are reported in Fig. 14 which displays the variation of the real and imaginary parts of ε_r as a function of frequency. Indeed as it was pointed out previously, there is no proper polarization direction for the magnetic field and as a consequence the basic cell exhibit an electric response rather than a magnetic one. At low frequency, a first resonance can be recorded with a well-resolved Lorentzian frequency variation. The resonance frequency is around 35 THz in agreement with the extinction peak measured and calculated in Fig. 13. The second one at 70 THz, which is more pronounced, also fits the second peak in Fig. 13 with a higher extinction ratio. Around 95 THz, a third resonance can be detected. However at this frequency, the imaginary part shows an opposite sign. Despite the good frequency agreement which can be noted also for this high spectral region the validity of the calculations becomes more questionable. In particular it is believed that the metamaterial condition ($d \ll \lambda$) become more and more difficult to justify.

With respect to the applications of a two-dimensional C-shaped array, one of the most interesting is to use them as anti-resonance filters since the optical beam can be sharply rejected at the various frequencies of plasmon resonators. The rejection, physically due to the evanescence of waves in a single negative medium—in the present case $\varepsilon_r < 0$, $\mu_r > 0$—can also be controlled by gating the gaps of SRR. The idea is basically simple and was used by many research groups in order to identify the electromagnetic effect resulting from Bragg or metamaterial effects. Indeed, by closing the ring, it can be demonstrated that the rejection peak disappears. This was often demonstrated by the fabrication of another sample of closed rings but it can also be envisaged to gate the C-shaped inclusion by illuminating the substrate. Photo creation or photodoping permits one to locally enhance the conductivity within the gap approaching the conductivity of metal. To the best of my knowledge, the experimental demonstration of such a tuneability of SRR-like array was solely demonstrated in the Far-Infra-Red [27]. At these frequencies, it is also possible to consider the electronic control of the rejection via the use of Schottly varactors. This is a complementary principle with respect to gating which consists to induce an overlap of the depleted regions between two adjacent metal semiconductor junctions.

Operation at NIR using metal nano-structures can also be envisaged. An excellent analysis of the route towards visible optics can be found in [28]. The basic underlying idea is to simplify as much as possible the shape of the patterns whose dimensions become shorter and shorter. For instance, a SRR operating around 0.8 μm should have a slit width less than 10 nm which is often the limit of resolution of commercially e-beam set-ups. More importantly, we

have to satisfy the proper polarization of the magnetic field. Let us recall that the direction of **H** has to be perpendicular to the SRR plane. An elegant way was proposed by Shalaev's group [29]. It is termed the double nanorods approach and it consists of tightly coupling two plasmon resonators [30]. It results from the coupling a lift of degeneracy of odd and even resonance modes. This means that the double rods metal inclusion show an electric and a magnetic moment which are, however, at different frequency bands while the achievement of a negative refractive index requires a DNG medium (ε_r and μ_r are negative in the same frequency band). In addition, both the dielectric and magnetic responses are Lorentzian. In order to overcome such a difficulty, the best route is to realize interconnected arrays. The so-called S-shaped and fishnet arrays belong to this category.

Let us now consider a full dielectric approach based on a Photonic Crystal (PC) technology [31,32]. This will permitted us to illustrate some specific applications of NRIM, notably negative refraction in prism-like devices and focusing using flat lens.

5. Negative index photonic crystal at Near-Infra-Red

Fig. 15 shows a SEM view of a two-dimensional photonic crystal aimed at operating at 1.5 μm. It consists of a hole array in a semi-conductor substrate. The scale (1 μm), indicated in this figure, show that the hole diameter and the pitch of the structure are on a submicron scale. In a first approximation they are comparable to $\lambda/4$ as in a one-dimensional Bragg mirror. Under this Bragg-condition, the device exhibits a forbidden gap which justifies the term Photonic Band Gap. For NRIMs, we do not take advantage of the gap but of the so-called folding of bands. It is known that the dispersion characteristics of periodic structures can be described by restricting the plot of ω–k function in the first Brillouin zone. Its boundaries are $k.a = \pm\pi$ where a is the pitch of the periodic structure. The full description of various eigen-modes of the photonic system can be performed by folding the bands. As a consequence, if the ground eigen-mode (Bloch wave mode) is right handed (group and phase velocities have the same sign), the second one is left handed. As a consequence PBGs can be used as NRIMs. One can find in Ref. [32] further details about the design rule and particularly how the band structures over the Brillouin zone are calculated, notably for satisfying the isotropy criteria.

With respect to the fabrication issue the general flow chart for fabricating NRIM using a PC technology consists of three major stages: (i) the growth of the semiconductor epilayers by molecular beam epitaxy; (ii) the nanoscale patterning by e-beam lithography; and (iii) the fabrication of hole array by induced couple plasma (ICP) or Deep Reactive Ion etching (DRIE).

The 2D confinement layer is ensured by a quaternary layer sandwiched between two InP layers in order to confine light at 1.5 μm in a direction transverse to the propagation direction. We choose the concentration of various elements (Ga(27%), In(73%), As(60%), P(40%)) so that the material is transparent at the wavelength of 1.5 μm and for lattice matching conditions. The thickness of this layer is 50 nm so that a monomode propagation can be expected in the frequency range of interest. The capping InP layer has a thickness of 20 nm. The confinement layer is thus relatively shallow with the goal to reduce as far as possible the depth of holes which will be subsequently etched. Indeed, a free surface with a high index contrast ($n_{\mathrm{InP}}/n_{\mathrm{Air}} = 3.3$) permits one to limit dramatically the spreading of the optical mode above the quaternary layer. In contrast the slight index difference between the confinement layer and the buried InP layer yields a large evanescence of waves toward the substrate and special attention has to be paid to the tail of optical mode in the substrate.

Electron-beam lithography is a necessary stage in order to pattern a mask transfer layer. In fact, a deep highly anisotropic etching (aspect ratio of 10:1 typically) is performed. It requires a mask which can *resist* the chemical etching by ions. This is the key role of this layer. In practice, we chose a Si_3N_4 film and high resolution lithography is used to transfer into this dielectric film the footprints of the array of holes with a low tolerance about the possible change in shape and dimension such as over-sizing of holes. To fabricate this mask transfer, we used PMMA (poly-methyl-methacrylate) resists as for the fabrication of SSRs discussed in Section 3. One of the key issue in the patterning of hole array or more generally of photonic crystal for nanophotonics is the correction of proximity effects. In short, forward and back scatterings spread the initial bunch of electrons. As a consequence, there is an increase of the zone which is written in practice with respect to the initial diameter of the electron spot. To overcome such a problem we used a multi-dose process on the basis of a simulation of diffusion of electron in the layered substrate. Further details can be found in [30]. Electron writing was carried of using high resolution pattern generator equipment (EBPG LEICA 5000) with a voltage of 50 kV.

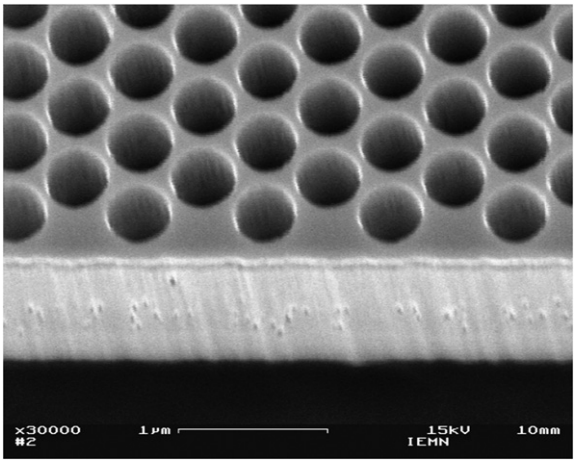

Fig. 15. Close up view of a hole array.

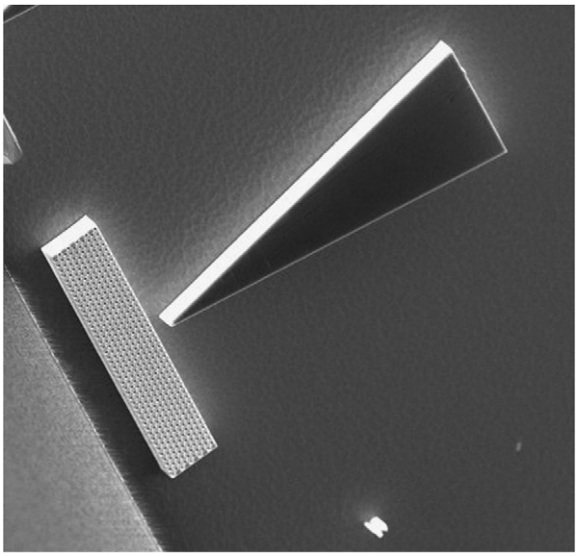

Fig. 16. SEM of a flat lens fed by a tapered optical waveguide.

The last stage in the fabrication of NRIMs is the deep etching of holes. For this purpose conventional Reactive Ion Etching (RIE) can be used with two main limitations. The first one was the rate of etching which was relatively low with respect to the depth. Indeed as mentioned previously, the tail of the wave-function is important towards the substrate. This can give rise to substrate propagation mode if the depth of hole is insufficient for the confinement of the optical mode in the transverse direction. Numerical simulations indicate that a hole depth of about 2 μm is enough for a good confinement. With respect to the hole diameter of this order of 200 nm, this means that etching has to be conducted not only on a sub-micron scale but also with an aspect ratio of the order of 10:1. The second disadvantage of RIE is the formation of carbon polymer during etching. We solved this problem by several plasma etchings during the process.

In order to increase the etching rate and also to solve the problem of polymers which act as micro-masks, we decided to develop etching by Inductively Couple Plasma (ICP) using an Oxford equipment (Plasma lab system 100). ICP power was 500 W, for an RF power of 75 W, a pressure of 4 mTorr and a table temperature of 20 °C. We used the following gas: CH_4(8 sccm), H_2(8 sccm) and Cl_2(8 sccm). After completing the etching (5 minutes duration) the Si_3N_4 thickness was measured to be 193 nm for an initial thickness of 225 nm. This means that the etching rate of Si_3N_4 is around 30 nm/minute. In contrast, a depth of 2 μm was achieved for the InP layer which yields an etching rate of 400 nm/minute. We thus obtained an etching selectivity of 13:1.

Fig. 16 shows a scanning Electron Micrograph of focusing device using a NRIM slab along with the tapered ridge waveguide (which acts as a point source). There is no micro-masking effect with grass-like pattern. The sidewalls of the ridge guide are very sharp and well-defined along with the hole array. The roughness of side wall is good along the round-shape and dimension of holes.

Fig. 17 shows the result of an electromagnetic simulation for a prism-like structure. We used here a square lattice. In practice, the propagation of electromagnetic waves is studied by means of the FDTD code Fullwave commercialized by Rsoft. The incident wave is injected on the left-hand side of prism at a wavelength of 1.5 μm. Within the prism-like nanostructure, it can be seen that the guided wavelength is larger than the relevant dimension of nanostructure. By marking the distance between two nodes an estimate of the guided wavelength is 5 μm which has to be compared to the relevant dimension of lattice (hole diameter 200 nm-period 300 nm). The incident wave injected perpendicular to the first interface does not suffer diffraction effect and keep the same direction as the one of incident wave. When the wave is impinging onto the second oblique interface the wave is strongly refracted. Both the travelling wave within the photonic crystal and the refracted beam have k directions in the same half plane defined by the normal at this interface (dashed line in this figure).

Fig. 18 shows the results for a PC slab. For the feeding we used a cut-ridge guide with a width of 300 nm apparent on the left-hand side of this figure. The reflection of waves on the first interface of the PC slab gives rise to a complex

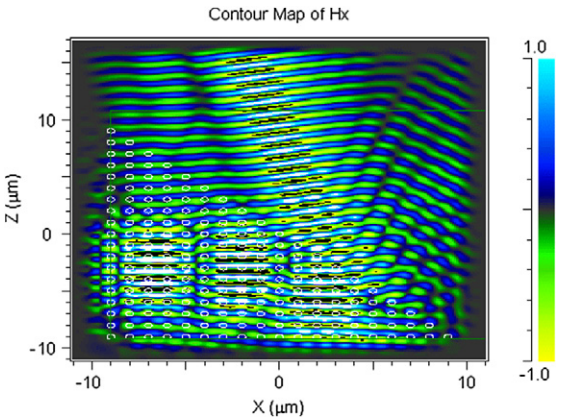

Fig. 17. Illustration of negative refraction in a prism-shaped NRIM (square lattice).

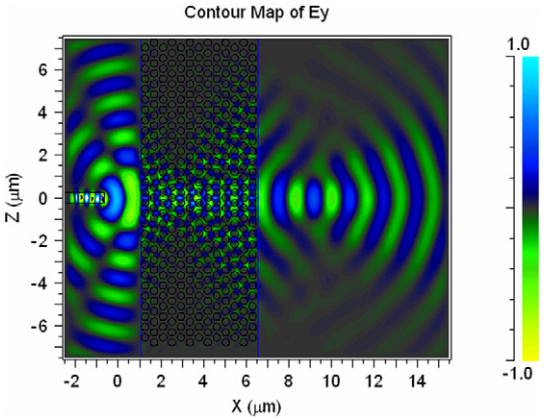

Fig. 18. Illustration of a focusing by a NRIM slab.

pattern in the vicinity of the injection region with a modulation of magnitude of electric field values of the order of the free space wavelength $\lambda = 1.5$ μm). It can be noted the formation of a first focus inside the lens as predicted in the seminal work of Veselago. As expected the guided wavelength is considerably reduced in the lens on a scale now comparable to the structuring dimension.

A second focus is formed outside the flat lens with relatively concentric iso-phases.

One can find in the literature the exciting idea that a NRIM lens is able to amplify the evanescent waves and thus to image a point source below the diffraction limit. The seminal work on this 'superlens' concept was published in [33] and was already demonstrated in DNG media at microwave [34] and in optics with SNGs, in practice a silver slab [35]. It is worth-mentioning that in the case of photonic crystals, it is difficult to satisfy the criterion of metamaterial (long wave range regime). In other words the wavelength is comparable and not much shorter than the relevant dimension. In conclusion, negative refraction can be observed, but it seems difficult by this route to overcome the diffraction limitation.

6. Conclusion and prospects

NRIM appears very promising in terms of application in the infra red spectral region owing to the openness of the parameters space. SNG and DNG micro- and nano-structures can now be fabricated over the whole infrared spectral region. The increase of the frequency of operation towards notably visible optics raises a number of theoretical difficulties related mainly to the dramatic increase of losses. The use of a PC technology can be a good alternative in order to alleviate these difficulties but some unique properties such as sub-wavelength imaging are lost. It is believed that the range of materials will be widened with the use of semiconductor (already introduced for PCs) and metal oxides. Also it is expected that the introduction of ferro-electrics or discrete devices will permit to introduce new functionalities such as tuneability at least in the lower part of the IR spectrum. At last, it seems that for a near future ultra-refractive metamaterials ($0 \leqslant \varepsilon_r, \mu_r < 1$) can bring new degrees of freedom for controlling electromagnetic waves. The demonstration of electromagnetic mirages and cloaking [36] is particularly representative of this recent evolution.

Acknowledgements

I would like to thank all the members of the DOME group along with the engineers and technicians of technological centre of IEMN whose help was determinant for the fabrication of metamaterials and PCs shown here. I am also grateful to G. Mouret, at The University du Littoral Dunkerque and J.F. Lampin at IEMN for the electro-optic sampling experiment at terahertz frequencies. The 100 GHz prototype was fabricated in Özbay group (University of Bilkent-Turkey). Many thanks for the loan of this prototype.

References

[1] V.G. Veselago, The electrodynamics of substances with simultaneously negative values of ε and μ, Sov. Phys. Usp. 10 (4) (1968).
[2] D.R. Smith, J.B. Pendry, M.C.K. Wiltshire, Science 10 (2004) 788–792.
[3] R.A. Shelby, D.R. Smith, S. Shultz, Experimental verification of a negative refraction index, Science 292 (2001) 77–79.
[4] J.B. Pendry, A.J. Holden, D.J. Robbins, W.J. Stewart, Magnetism from conductors and enhanced nonlinear phenomena, IEEE Trans. Microwave Theory Tech. 47 (11) (1999).
[5] J.B. Pendry, A.T. Holden, W.J. Stewart, I. Youngs, Extremely low frequency plasmons in metallic mesostructures, Phys. Rev. Lett. 76 (1996) 4773.
[6] G.V. Eleftheriades, A.K. Iyer, P.C. Kremer, Planar negative refractive index media using periodically L–C loaded transmission lines, IEEE Trans. Microwave Theory Tech. 50 (12) (2002).
[7] A. Grbic, V. Eleftheriades, Experimental verification of backward-wave radiation from negative refractive index metamaterials, J. Appl. Phys. 92 (10) (2002).
[8] C.G. Parazzoli, R.B. Greegor, K. Li, B.E.C. Koltenbah, M. Tanelian, Experimental verification and simulation of negative index of refraction using Snell's law, Phys. Rev. Lett. 90 (2003) 107401.
[9] S.O. Brien, D. McPeake, S.A. Ramakrishna, J. Pendry, Near-infrared photonic band gap and non linear effects in negative magnetic materials, Phys. Rev. B 69 (2004) 241101.
[10] H.O. Moser, B.D.F. Cassa, O. Wilhemi, B.T. Saw, Terahertz response of a microfabricated Rod-Split Ring Resonator Electromagnetic Metamaterials, Phys. Rev. Lett. 94 (2005) 063901.
[11] D.R. Smith, J.B. Pendry, M.C.K. Wiltshire, Metamaterials and negative refractive index, Science 305 (2004) 788–792.
[12] R. Moussa, S. Foteinopoulou, L. Zhang, G. Tuttle, K. Guven, E. Ozbay, C.M. Soukoulis, Negative refraction and superlens behavior in a two-dimensional photonic crystal, Phys. Rev. B 71 (2005) 085106.
[13] M. Bayindir, K. Aydin, E. Ozbay, P. Markos, C.M. Soukoulis, Transmission properties of composite metamaterials in free space, Appl. Phys. Lett. 78 (2002) 489–491.
[14] T. Decoopman, O. Vanbésien, D. Lippens, Demonstration of a backward wave in single split ring resonator and wire loaded finline, IEEE Microwave Opt. Tech. Lett. 14 (2004) 507–509.
[15] T. Decoopman, A. Marteau, E. Lheurette, O. Vanbésien, D. Lippens, Left-handed electromagnetic properties of split-ring resonator and wire loaded transmission line in a fin-line technology, IEEE Trans. Microwave Theory Techniques 45 (4) (2006) 1451–1457.
[16] J. Carbonell, L.J. Rogla, V. Boria, D. Lippens, Design, and experimental verification of backward wave propagation in periodic waveguide structures, IEEE Trans. Microwave Theory Techniques 54 (4) (2006).
[17] R. Marques, F. Mesa, J. Martel, F. Medina, Comparative analysis of edge- and Broadside coupled split ring resonators for metamaterial-design theory and experiments, IEEE Trans. Antennas Propagation 51 (10) (2003) 2572–2581.
[18] P.F. Loschiolpo, D.L. Smith, D.W. Forester, F.J. Rachford, J. Schelleng, Electromagnetic waves focused by a negative-index planar lens, Phys. Rev. E 67 (2003) 025602.
[19] E. Lheurette, O. Vanbésien, D. Lippens, Double negative media using interconnected omega-type metallic particles, Microwave Opt. Tech. Lett. 49 (1) (2007).
[20] D. Lippens, Electromagnétisme des matériaux gauchers, Techniques de l'ingénieur, dossier RE 63, 2005.
[21] D. Lippens, Réfracter la lumière à l'envers, Pour la Science 345 (2006) 68–74.
[22] M. Gokkavas, K. Guven, I. Bulu, K. Aydin, R.S. Penciu, M. Kafesaki, C.M. Soukoulis, E. Ozbay, Experimental demonstration of a left-handed metamaterial operating at 100 GHz, Phys. Rev. B 73 (2006) 193103.
[23] D.R. Smith, S. Schultz, P. Markos, C.M. Soukoulis, Determination of effective permittivity and permeability of metamaterials from reflection and transmission coefficients, Phys. Rev. Lett. 65 (2002) 195104.
[24] J.M. Lerat, N. Malléjac, O. Acher, Determination of effective parameters of a metamaterial by field summation method, J. Appl. Phys. 100 (2006) 1–9.
[25] T. Crépin, J.F. Lampin, T. Decoopman, X. Mélique, L. Desplanque, D. Lippens, Experimental evidence of backward wave on terahertz left-handed transmission lines, Appl. Phys. Lett. 87 (10) (2005), 104105-1-3.
[26] S.O. Brien, J.B. Pendry, Magnetic activity at infrared frequencies in structures metallic photonic crystals, J. Phys. Condens. Matter 14 (2002) 6383–6394.
[27] W.J. Padilla, A.J. Taylor, C. Highstrete, M. Lee, R.D. Averitt, Dynamical electrical and magnetic metamaterial response at terahertz frequencies, Phys. Rev. Lett. 96 (2006) 107401.
[28] S. Linden, C. Enkrich, M. Wegener, J. Zhou, T. Koschny, C. Soukoulis, Magnetic response of metamaterials at 100 THz, Science 306 (2004) 1351–1354.
[29] V. Podoskiy, A.K. Sarychev, V.M. Shalaev, Plasmon modes and negative refraction in metal nanowire composite, Opt. Express 11 (2003) 735–745.
[30] A.N. Grigorenko, A.K. Geim, H.F. Gleeson, Y. Zhang, A.A. Firsov, I.Y. Khrushchev, J. Petrovic, Nanofabricated media with negative permeability at visible frequencies, Nature 43 (2005) 335–338.
[31] M. Perrin, S. Fasquel, T. Decoopman, X. Mélique, O. Vanbésien, E. Lheurette, D. Lippens, Left handed electromagnetism obtained via nanostructures metamaterials: comparison with that from microstructured photonic crystals, J. Opt. A: Pure Appl. Opt. 7 (2005) S3–S11.
[32] S. Fasquel, X. Mélique, O. Vanbésien, D. Lippens, Three dimensional calculation of propagation losses in photonic, Crystal Waveguides Opt. Commun. 246 (1–3) (2005) 91–96.
[33] J.B. Pendry, Negative refraction makes a perfect lens, Phys. Rev. Lett. 85 (2000) 3966–3969.
[34] A. Grbic, G.V. Eleftheriades, Overcoming the diffraction limit with planar left-handed transmission lens, Phys. Rev. Lett. 92 (2004) 117403.
[35] N. Fang, H. Lee, C. Sun, X. Zhang, Subdiffraction-limited optical imaging with a silver superlens, Science 308 (2005) 534–537.
[36] J.B. Pendry, D. Shurig, D.R. Smith, Controlling electromagnetic waves, Science-express, www.sciencexprss.orgt/25May2006/page1/10.1126/science.1125907.